Progress on the Development of a Simulation Environment for Optical Communications

Joel Shields[a], Meera Srinivasan[a], Martin W. Regehr[a]

[a]Jet Propulsion Laboratory, California Institute of Technology, 4800 Oak Grove Blvd., Pasadena, CA, USA;

ABSTRACT

Deep space laser communications require extremely accurate beam pointing to take advantage of the narrow beams achievable at optical wavelengths. This pointing accuracy must be achieved in the presence of spacecraft basebody motion which may exceed laser pointing requirements by orders of magnitude.

In this paper a model of an optical band transceiver pointing control system is developed that can be used to predict performance under various operating scenarios. The transceiver model consists of an electro-mechanical model of the telescope platform and isolator. A novel photon counting detector array is used in the simulation as the focal plane detector. In the simulation we are able to inject various cases of spacecraft basebody motion based on both flight data and future mission spacecraft jitter requirements. Various models of uplink beacon flux levels and atmospheric scintillation are also available for analysis.

Using these models, detector processing and control functions are implemented in the simulation. A complete acquisition sequence is demonstrated with blind acquisition and tracking of the modulated uplink beam and positioning of the downlink beam on the focal plane array. These simulations predict that pointing requirements will be met with representative disturbance models and uplink beam scintillation.

Keywords: Optical communications, isolator, fast steering mirror, pointing control, acquisition, tracking, centroiding

1. INTRODUCTION

Optical communication technology offers data rates much higher than those of conventional radio frequency (RF) based technology. These data rates are made possible through the large signal to noise ratios that are possible with narrow optical band beam widths. Many optical communication scenarios have been demonstrated in the past including ground to ground,[1] aircraft to ground,[2] ground to Earth orbit,[3] and inter-orbit[4] communication links. In this paper, we are primarily concerned with deep space optical communications between a spacecraft orbiting a planetary body such as Mars and an Earth station such as the Large Binocular Telescope (LBT), Optical Communications Telescope Laboratory (OCTL) or other large aperture optical telescope. Though a number of efforts have been put forth on the system engineering of deep space optical transceivers,[5–7] to our knowledge relatively little effort has been made in developing an end to end simulation capability for these systems. This paper attempts to bridge this gap. We believe by doing so, the complex interactions between the various subsystems, which can be interdisciplinary in nature, can be understood at a deep level. Moreover, the simulation can be used to develop requirements on these subsystems, address issues with different mission proposals including L2, Jupiter, and space to space missions and to support various trade studies. Examples of these trade studies include determining the amount of allowable basebody motion, evaluation of the necessary isolation to reaction wheel modes, determining the necessary uplink beacon irradiance, determining operational wind speeds, determining the necessary sample rates on the control and estimation algorithms, and evaluation of various detector types. A byproduct of these sorts of investigations would be prototype flight code for detection and tracking.

Further author information: (Send correspondence to Joel F. Shields)
Joel F. Shields: E-mail: Joel.F.Shields@jpl.nasa.gov, Telephone: 1 818 354 2376

A key component of this technology is accurate and stable pointing of the uplink and downlink lasers. Various pointing operations are required to first establish an optical link then to maintain it in the presence of various events or disturbances that can break the link. The scope of this simulation effort assumes that some prior calculations and operations have been performed that have successfully illuminated the spacecraft with the uplink beam. Furthermore, we assume that a two axis gimbal system on the spacecraft has been used to point the boresight of the transceiver's telescope in such a way that the uplink beam is close or within the field of view (FOV) of the telescope. The simulation then starts with a search and detection of the uplink beam and ends with tracking of both the uplink and downlink beams at specific target locations on the focal plane array. A mode commander is used by the simulation to coordinate this process using three different modes or configurations of the detector subwindows. A key input into the mode commander is a detection flag for the uplink beam generated by the detector processing software.

To achieve the pointing requirements for this application a telescope isolation system has been developed.[8] Prototypes of this system have been built at JPL. The system is used to isolate the transceiver telescope from various disturbance sources on the spacecraft bus. We developed a model of this system using appropriate mass properties and including voice coils and local sensors known at JPL as "LVDTs". These sensors differ from conventional LVDTs in that, instead of having a moving core, they have a primary which moves axially relative to a coaxial secondary. The stiffness of a connecting umbilical is also included in the isolator model. Models of the basebody disturbance, uplink beam scintillation, and optical sensitivities are also developed in this paper.

The baseline flight terminal architecture[9] utilizes a single photodetector array for uplink signal acquisition, tracking, and data detection in order to minimize optical losses as well as mass and power on the spacecraft. The design also calls for the focal plane sensor to simultaneously detect both the downlink transmit and uplink receive beams on a 128x128 pixel photon counting detector (PCD) array. While CCD arrays may also be viable cost-effective alternatives to the photon counting array, overall acquisition and tracking performance may be degraded substantially by their lower readout rates and less favorable noise characteristics. A model of the PCD and its readout electronics is used in the simulation. These devices are new, but small size arrays are currently manufactured. The PCD array requires development of custom readout circuitry, which in turn imposes restrictions upon the signal processing algorithms needed for signal acquisition and tracking. These details are described in the detector modeling subsection below.

The simulation is implemented in a Matlab/Simulink environment with C and C++ "sfunctions" used for most of the algorithms and models. We used a software package called SDFAST to generate the equations of motion of the mechanical model components. This software package generates C code for integrating the equations of motions of complex interconnected multibody systems subject to various forces and torques applied to the bodies. The code is generated from a simple system description file. In the discussion and notation that follows we sometimes refer to the uplink beam as the receive beam (RB) and the downlink beam as the transmit beam (TB).

2. MODELING

2.1 Mechanical Modeling

The mechanical model used in the simulations is shown in Figure 1a and 1b. The model consisted of five bodies in a tree configuration. The basebody, or spacecraft bus, is a prescribed motion body. SDFAST provides utilities for prescribing the motion of any particular body. The linear position and velocity of the center of mass of this body are set to zero and the angular position and velocity are based on a trajectory selected from those described in Section 2.3 below. This avoids the necessity of modeling the attitude control system (ACS) of the spacecraft since the net motion of the spacecraft to various sensor noises and disturbance events are captured in the trajectory. The two gimbal joints are both 1 degree of freedom (DOF) pin joints and are used to perform coarse pointing of the transceiver platform. The fourth body in the tree is the platform, or telescope, body. It is connected to the outer gimbal body by a free joint. An umbilical is used to transfer electrical power, data and laser power between the telescope and spacecraft. This umbilical adds stiffness between these two bodies. The stiffness and damping of this mechanical interface was experimentally tested[10] and included in the mechanical model. There are also six voice coil actuators between the outer gimbal body and the platform body. These

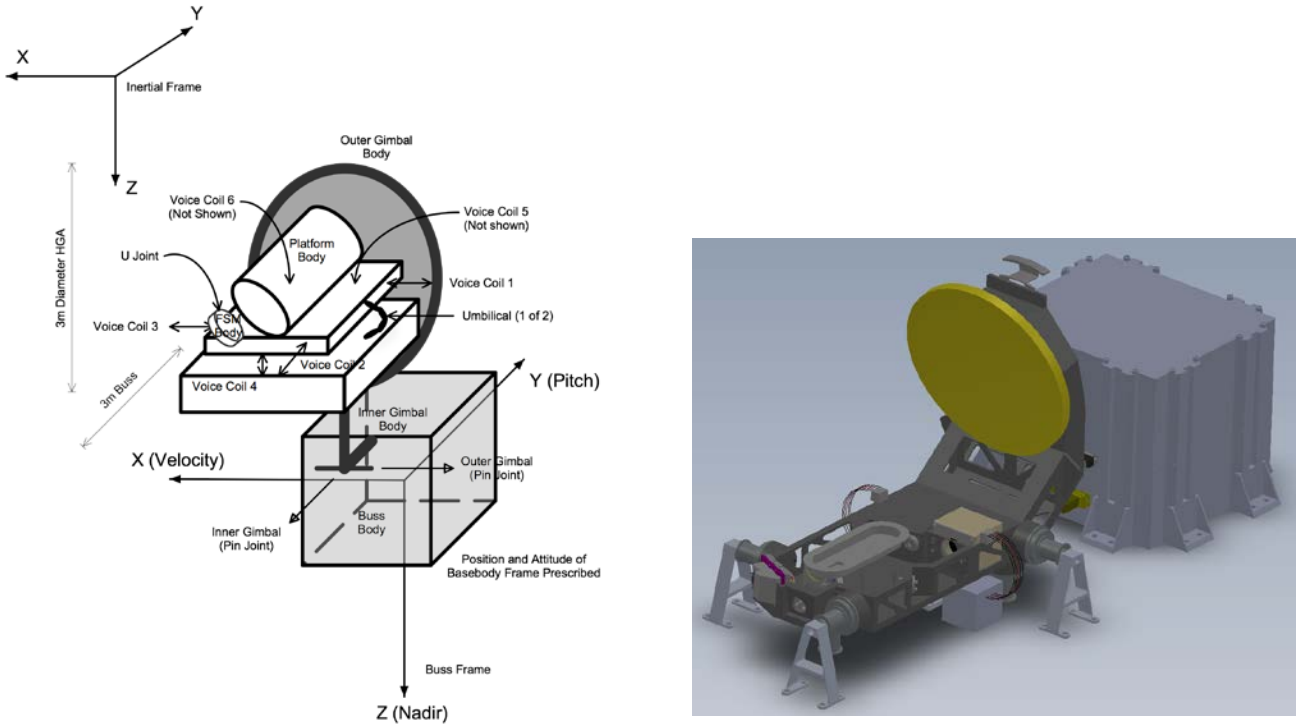

Figure 1. (a) Multibody model of spacecraft and transceiver terminal in the reference configuration with each body frame aligned with the inertial frame. (b) Transceiver platform showing umbilical attachments and voice coil actuators.

actuators are used to point the telescope in pitch and yaw and to prevent contact between these two bodies. Three of the actuators can be seen in Figure 1b. Three more are placed below the platform. The local LVDT sensors are collocated with each voice coil giving local feedback on the position and orientation of the platform relative to the outer gimbal. The last body in the tree configuration is the FSM which is connected to the platform via a 2 DOF u-joint. The inputs into the mechanical model are the two gimbal joint torques, the two FSM torques and the 6 linear voice coil forces. The outputs consist of the joint position and velocity coordinates between each body which total 18. These include the basebody linear position and velocity and the basebody quaternion and angular velocity. All of these DOFs are prescribed. The gimbal angles and angular velocities are also output as well as the platform linear position and velocity, quaternion and angular rate vector. The FSM u-joint angles and angular rates are also output. In addition, the inertial position and quaternions of each body were also output. This was done to simplify the data input into the optical model. Representative mass and inertia properties were selected from the Mars Reconnaisance Orbiter (MRO) spacecraft and the platform prototype developed by Gerry Ortiz.[11]

2.1.1 Local Sensor Modeling

Each of the six voice coils is parameterized as having a location on the outer gimbal body and a line of action or direction in this frame. Let the locations with respect to the center of mass of the outer gimbal be given by $\mathbf{v}^{OGF}_{vc1_{ogcm}}, \ldots, \mathbf{v}^{OGF}_{vc6_{ogcm}}$ and their directions by $\hat{\mathbf{u}}^{OGF}_{vc1}, \ldots, \hat{\mathbf{u}}^{OGF}_{vc6}$. The local sensors are collocated with the actuators and measure the linear displacements along each voice coil direction. To model these measurements the platform displacements at each of the six voice coil locations are mapped to the outer gimbal frame and projected onto the voice coil line of action. The input into the model are the relative joint coordinates between the platform and outer gimbal bodies. These coordinates are the quaternion, $\mathbf{q}_{platform}$, giving the orientation of the platform frame relative to the outer gimbal frame and the translation $\mathbf{v}^{OGF}_{platform}$ of the hinge point of the free joint "connecting" these two bodies. These two variables are output from the SDFAST dynamics engine. To calculate the displacements we first determine the voice coil locations with respect to the platform center of

mass,

$$\mathbf{v}^{OGF}_{vc1_{pcm}} = \mathbf{v}^{OGF}_{vc1_{ogcm}} - (\mathbf{v}^{OGF}_{inb2joint} - \mathbf{v}^{OGF}_{body2joint}), \tag{1}$$

where $\mathbf{v}^{OGF}_{inb2joint}$ and $\mathbf{v}^{OGF}_{body2joint}$ are the vectors from the outer gimbal body center of mass to the free joint location and from the platform body center of mass to the free joint location, respectively. The location of this same point on the platform after translation and rotation of the free joint is given by,

$$\mathbf{v}^{OGF}_{vc1^{t}_{ogcm}} = \mathbf{v}^{OGF}_{inb2joint} + \mathbf{v}^{OGF}_{platform} + \mathbf{C}(\mathbf{q}^{*}_{platform})(\mathbf{v}^{OGF}_{vc1_{pcm}} - \mathbf{v}^{OGF}_{body2joint}), \tag{2}$$

where $\mathbf{q}^{*}_{platform}$ is the complex conjugate of $\mathbf{q}_{platform}$. We then take the difference between $\mathbf{v}^{OGF}_{vc1^{t}_{ogcm}}$ and $\mathbf{v}^{OGF}_{vc1_{ogcm}}$ and project it onto $\hat{\mathbf{u}}^{OGF}_{vc1}$,

$$s_1 = (\mathbf{v}^{OGF}_{vc1^{t}_{ogcm}} - \mathbf{v}^{OGF}_{vc1_{ogcm}})^{T}\hat{\mathbf{u}}^{OGF}_{vc1}, \tag{3}$$

where s_1 is the displacement sensed along the first voice coil line of action. Equations (1)-(3) are repeated for sensors 2 through 6. Also included in the sensor model is measurement noise that is added to each displacement. According to lab tests, the local sensors have 1.0 $nm/\sqrt{Hz}$ white noise.

For local control of the platform we need the inverse sensor Jacobian. This is the sensitivity between changes in the sensor measurements, $\Delta s_1, \ldots, \Delta s_6$, to changes in the joint coordinates $\Delta x, \Delta y, \Delta z, \Delta\theta_x, \Delta\theta_y, \Delta\theta_z$. If we denote $\mathbf{s} = \mathbf{f}(\mathbf{u})$ with $\mathbf{u} = [\Delta x, \Delta y, \Delta z, \Delta\theta_x, \Delta\theta_y, \Delta\theta_z]^T$ and $\mathbf{s}$ as the vector of local sensor displacements, this sensitivity was determined by taking the inverse of,

$$\left.\frac{\partial \mathbf{f}}{\partial \mathbf{u}}\right|_{\mathbf{0}}, \tag{4}$$

which was itself calculated using a central difference technique. We denote the inverse of this sensitivity as $\mathbf{K}_{pose}$.

2.1.2 Actuator Jacobian

The control loops will also require the mapping from forces and torques on the platform to the individual voice coil forces. As shown in Figure 4 below, this is needed for local control of the platform, open loop searching with the platform and for control of the platform under uplink beam detector feedback. This mapping is derived for the case when $\mathbf{v}^{OGF}_{platform} = [0\ 0\ 0]^T$ and $\mathbf{q}_{platform} = [0\ 0\ 0\ 1]^T$. In this configuration each voice coil will produce a force and torque on the platform body according to,

$$\begin{bmatrix}\mathbf{f}^{OGF}\\ \boldsymbol{\tau}^{OGF}\end{bmatrix} = \underbrace{\begin{bmatrix}\hat{\mathbf{u}}^{OGF}_{vc1} & \cdots & \hat{\mathbf{u}}^{OGF}_{vc6}\\ (\mathbf{v}^{OGF}_{vc1_{pcm}} - \mathbf{v}^{OGF}_{body2joint}) \times \hat{\mathbf{u}}^{OGF}_{vc1} & \cdots & (\mathbf{v}^{OGF}_{vc6_{pcm}} - \mathbf{v}^{OGF}_{body2joint}) \times \hat{\mathbf{u}}^{OGF}_{vc6}\end{bmatrix}}_{\mathbf{K}^{-1}_{vcf}} \begin{bmatrix}f_{vc1}\\ f_{vc2}\\ f_{vc3}\\ f_{vc4}\\ f_{vc5}\\ f_{vc6}\end{bmatrix}. \tag{5}$$

The desired transformation is just the inverse of this relationship which we denote as $\mathbf{K}_{vcf}$.

2.2 Optical Modeling

The optical model takes the motion of the FSM and platform and outputs the focal plane position of the uplink and downlink beams and the inertial direction of the downlink link. The FSM orientation is parameterized inside SDFAST with two angles about each of the u-joint degrees of freedom. The platform orientation is output from SDFAST in terms of a quaternion, $\mathbf{q}_{IF2PF}$, that passively maps inertial frame vectors into the platform frame. To get the uplink beam focal plane position we first map the inertial direction of this beam into the platform frame,

$$\hat{\mathbf{i}}^{PF}_{RB} = \mathbf{C}(\mathbf{q}_{IF2PF})\hat{\mathbf{i}}^{IF}_{RB}, \tag{6}$$

where $\hat{\mathbf{i}}^{IF}_{RB}$ is the chosen inertial direction of this beam and $\mathbf{C}(\mathbf{q}_{IF2PF})$ is the direction cosine matrix associated with the quaternion $\mathbf{q}_{IF2PF}$. The direction of this beam in the platform frame is then mapped to detector coordinates,

$$\mathbf{v}_{RB} = \mathbf{K}_{OS}\begin{bmatrix}-\theta_{AZ}\\ -\theta_{EL}\end{bmatrix} + \begin{bmatrix}64\\ 64\end{bmatrix}, \tag{7}$$

where,

$$\mathbf{K}_{OS} = \begin{matrix} 1/8e-6 & 0 \\ 0 & 1/8e-6 \end{matrix} \tag{8}$$

is the optical sensitivity of the telescope in pixels per radian and the angles θ_{AZ} and θ_{EL} are given by,

$$\theta_{AZ} = atan2(\hat{\mathbf{i}}(x)_{RB}^{PF}, \hat{\mathbf{i}}(y)_{RB}^{PF}) \tag{9}$$

$$\theta_{EL} = atan2\left(\hat{\mathbf{i}}(z)_{RB}^{PF}, \sqrt{\hat{\mathbf{i}}(x)_{RB}^{PF\,2} + \hat{\mathbf{i}}(y)_{RB}^{PF\,2}}\right). \tag{10}$$

The vector at the end of equation (7) is added to bias the beam position to the center of the detector when the incident beam direction in inertial coordinates is coaligned with the y-axis of the platform body, also taken as the boresight direction. To get the downlink beam focal plane position we first determine the FSM normal given the FSM joint coordinates, θ_{FSM1} and θ_{FSM2},

$$\hat{\mathbf{n}}^{PF} = exp(\hat{\mathbf{u}}_{pin1}^{PF} \times \theta_{FSM1})\hat{\mathbf{n}}^{PF} \tag{11}$$

$$\hat{\mathbf{u}}_{pin2}^{PF} = exp(\hat{\mathbf{u}}_{pin1}^{PF} \times \theta_{FSM1})\hat{\mathbf{u}}_{pin2}^{PF} \tag{12}$$

$$\hat{\mathbf{n}}^{PF} = exp(\hat{\mathbf{u}}_{pin2}^{PF} \times \theta_{FSM2})\hat{\mathbf{n}}^{PF} \tag{13}$$

where $\hat{\mathbf{u}}_{pin1}^{PF}$, $\hat{\mathbf{u}}_{pin2}^{PF}$ and $\hat{\mathbf{n}}^{PF}$ are the FSM pin joint unit vectors and mirror normal when the joint coordinates are zero. The new mirror normal, $\hat{\mathbf{n}}^{PF}$, is then used to reflect the incident downlink beam direction, $\hat{\mathbf{i}}_{TB}^{PF}$,

$$\hat{\mathbf{r}}^{PF}_{TB} = (\mathbf{I} - 2\hat{\mathbf{n}}^{PF}\hat{\mathbf{n}}^{PF\,T})\hat{\mathbf{i}}_{TB}^{PF} \tag{14}$$

to get the direction of the downlink beam reflected off the FSM. This reflected beam is transformed into a "reflected" frame formed from,

$$\mathbf{T}_{PF2RF} = \begin{bmatrix} \hat{\mathbf{y}}^{PF\,T} \\ \hat{\mathbf{x}}^{PF\,T} \\ \hat{\mathbf{z}}^{PF\,T} \end{bmatrix}, \tag{15}$$

where $\hat{\mathbf{y}}^{PF}$ is the reflected unit vector formed from Equation (14) with the unchanged normal vector $\hat{\mathbf{n}}^{PF}$. $\hat{\mathbf{z}}^{PF} = [0\ 0\ 1]^T$ and $\hat{\mathbf{x}}^{PF\,T}$ is the cross product of $\hat{\mathbf{y}}^{PF\,T}$ with $\hat{\mathbf{z}}^{PF\,T}$. The azimuth and elevation angles are computed in this frame in a manner similar to Equations (9) and (10),

$$\theta_{AZ} = atan2(\hat{\mathbf{r}}(x)_{TB}^{RF}, \hat{\mathbf{r}}(y)_{TB}^{RF}) \tag{16}$$

$$\theta_{EL} = atan2\left(\hat{\mathbf{r}}(z)_{TB}^{RF}, \sqrt{\hat{\mathbf{r}}(x)_{TB}^{RF\,2} + \hat{\mathbf{r}}(y)_{TB}^{RF\,2}}\right). \tag{17}$$

These angles are then mapped to detector coordinates as before with,

$$\mathbf{v}_{TB} = \mathbf{K}_{OS}\begin{matrix} -\theta_{AZ} \\ -\theta_{EL} \end{matrix} + \begin{matrix} 64 \\ 64 \end{matrix} + \begin{matrix} 26 \\ 26 \end{matrix}, \tag{18}$$

where the additional offset is introduced by a fold mirror prior to the detector. This fold mirror acts to separate the uplink and downlink beams on the focal plane when they share the same direction on the sky. The separated locations allows easier centroiding.

To get the inertial direction of the downlink beam we first transform $\hat{\mathbf{r}}_{TB}^{RF}$ back into the platform frame assuming that the frame *RF* is coaligned with the frame *PF* with the exception that the +y-axis of the *RF* frame points in the -y-axis of the *PF* frame. This accounts for the direction change associated with the last reflection off the primary. The direction of the inertial frame downlink vector is then given by,

$$\hat{\mathbf{r}}_{TB}^{IF} = \mathbf{C}(\mathbf{q}_{IF2PF}^{*})\hat{\mathbf{r}}_{TB}^{PF}, \tag{19}$$

where we then use equations similar to (16) and (17) to get inertial azimuth and elevation angles.

To summarize, moving the platform in pitch and yaw is used to position the uplink beam on the focal plane in the y and x directions respectively. By proxy the platform motion also moves the downlink beam inertially since it is launched from inside the platform body. Moving the FSM about its two articulation axes is used to position the downlink beam on the focal plane and to move it inertially. Although the above treatment is generic the incident downlink beam on the FSM is chosen to be nearly normal (22.5 degrees) giving Equations (16) and (17) a sensitivity of 2 to the FSM joint coordinates θ_{AZ} and θ_{EL}.

2.3 Disturbance Modeling

The disturbance that the transceiver terminal is subject to is injected into the simulation as inertial attitude motion of the spacecraft basebody. To prescribe this motion, SDFAST requires the bus attitude, angular velocity, and angular acceleration. Since only attitude data was available, the velocity and acceleration had to be generated numerically. Smoothing and causal numerical differentiation techniques were used to ensure that the derivatives were consistent.

Flight data from the MRO spacecraft[12] is used to prescribe this motion as well as the disturbance specifications based on the Mars Laser Communications Demonstration (MLCD) mission.[6] Several MRO disturbance scenarios can be selected. Two “on orbit” cases and one “cruise” stage case. The two on orbit cases exhibit much larger attitude perturbations due to various events that occur during the orbit. These events include reaction wheel desats and other thruster events, solar panel repositioning, high gain antenna (HGA) slews and commanded off nadir roll maneuvers. The cruise data is much quieter and more predictable.[12] The data injected into the simulation as basebody motion was the ACS error, or the difference between the commanded attitude of the spacecraft and the estimated attitude generated by the attitude determination (AD) filter which mixes the star tracker and gyro measurements in an optimal fashion. The first on orbit case uses the raw time domain flight data which was available at 5 Hz. This data is characterized by spurious events on the order of ±1.0 milliradian in each of the three attitude degrees of freedom. As with all other cases, if the simulation requires disturbance data at a time in between the samples, Simulink automatically performs a linear interpolation. A second on orbit case is available that gives a much higher frequency model of the spacecraft basebody attitude. In this data set high rate gyro data augmented the ACS data to give a high frequency model of spacecraft motion. This model revealed several high frequency modes between 10 and 100 Hz associated with reaction wheel imbalances. A shaping filter was fit to the PSD of this combined data set. The output of this shaping filter is available at a 200 Hz rate. This case is good for testing the performance of the platform isolator at high frequencies. The MRO cruise data is based on raw data and is available at 1 Hz. The MLCD data is generated from a shaping filter fit to the PSD requirement for this mission. This data is available at 200 Hz.

For all of these scenarios most of the disturbance power in is in the 0.01 to 0.03 Hz range. In terms of amplitude the equivalent focal plane motion for these scenarios is roughly equal to the diameter of the focal plane assuming 8.0 microradians per pixel and a 128x128 pixel array. Note that the platform isolator is subject to both rotational and translational disturbances due to the large, ~3 meter, lever arm between the basebody center of mass and transceiver location. This effect is captured in the multibody model.

2.4 Scintillation Modeling

The uplink beacon is subject to intensity variations caused by its travel through the Earths atmosphere. These intensity variations have been modeled as part of a larger link budget.[13] In order to mitigate the signal fading caused by these intensity variations, multiple co-propagating uplink beams of mutually incoherent lasers may be employed. Both 1 beam and 8 beam scintillation cases can be used in the simulation. These cases differ in the variation between the maximum and minimum brightness. For the 1 beam cases the intensity variations are generally 20 dB greater than the 8 beam cases because of the reduced aperture. The zenith angle for all cases is 70 degrees and the range is assumed to be 2.4 AU. Cases for a 20 microradian beam, 40 microradian beam, and 20 microradian beam with 7.5 microradians of offset are all available. Data files are provided in units of Watts per square meter per Watt transmitted and converted to flux in photons per second with assumptions on the aperture of the telescope, transmitted power, detector efficiency, optical receiver loss, and various physical constants. The data files are sampled at 1000 Hz and a linear interpolation is performed in the simulation if data between samples is required.

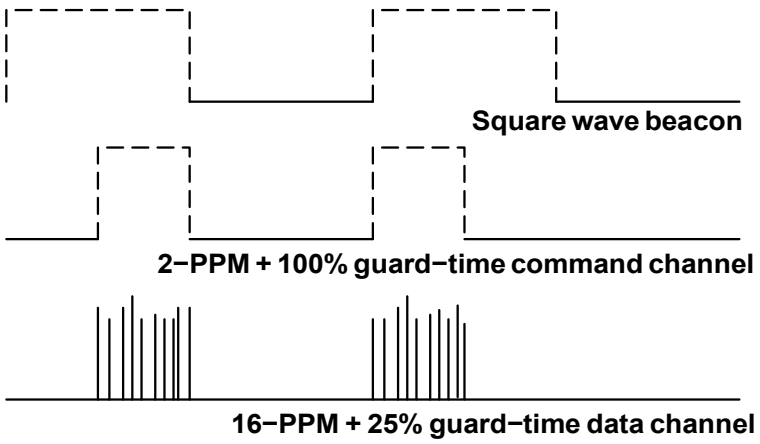

Figure 2. Nested uplink modulation signal structure

2.5 Uplink Signal and Detector Output Modeling

Acquisition of the received signal at the flight terminal consists of several components: spatial signal detection to determine whether the uplink optical signal beam is on the photodetector array, centroiding to estimate the beam location and to provide feedback to the pointing and control system, and temporal acquisition of the uplink data symbols. In addition, the transmitted downlink signal pointing is implemented using the detector array as well by reflecting a portion of the downlink beam onto the flight detector array. The simulation developed to date focuses upon the spatial acquisition and tracking aspects of the problem and does not yet address temporal synchronization.

To accomodate pointing, acquisition, and tracking of the received signal as well as data detection, a novel nested uplink modulation format has been proposed[9] consisting of a low-bandwidth command channel and a higher bandwidth variable rate data channel. The higher rate inner modulation consists of order 16 pulse position modulation (16-PPM) plus four intersymbol guard time slots, while the lower rate outer modulation consists of 2-PPM with two intersymbol guard-time slots (see Figure 2). This combination results in an average square wave pattern that may be exploited for background rejection and signal acquisition. Specifically, by alternately incrementing and decrementing a photon arrival counter that is aligned to the square wave beacon, we subtract out background counts (assumed to be constant over some time interval) while collecting signal counts, thereby improving statistics for signal detection and centroid estimation. Moreover, by using two such up-down counters offset by one-quarter of the square wave period, temporal synchronization of the counters with the received signal is not needed. These up-down counters comprise a key component of the signal acquisition strategy described in this paper.

Let $\lambda_{s,I}$ and $\lambda_{b,I}$ be the mean signal and background intensities absorbed by a single photodetector pixel indexed by I, let T_s be the command channel slot duration, and let N be the number of periods of the beacon square wave contained in some integration time T_{int}. If the overall average photon intensity absorbed by a single photon-counting pixel is λ, then the number of photoelectrons counted over time T_s is Poisson distributed with parameter λT_s. If we let U_I and V_I be random variables representing the up-down counter statistics collected over time $T_{int} = N T_s$ from the I^{th} detector pixel, then U_I and V_I may be approximated as Gaussian random variables with means and variances

$$E[U_I] = 4N(1 - E)\lambda_{s,I} T_s, \qquad Var[U_I] = 4N(\lambda_{b,I} + \lambda_{s,I})T_s \tag{20}$$

$$E[V_I] = 4NE\lambda_{s,I} T_s, \qquad Var[V_I] = 4N(\lambda_{b,I} + \lambda_{s,I})T_s \tag{21}$$

where E is the time offset of the up-down counters with respect to the beginning of the slot, as a fraction of the slot duration ($0 \le E < 1$). A near-optimal statistic for signal detection is then conjectured to be given by $W_I = U_I^2 + V_I^2$. While the expected value of each up-down counter statistic only depends upon the signal intensity

and not background, the expected values of the square-law statistic W_l do depend upon the background intensity. If in addition to the up-down counters, we also have an up-counter S_l for each pixel, an alternate statistic W'_l may be given by $W'_l = U'^2_l + V'^2_l - 2S_l$. The dependence upon background intensity is removed in the the expected value of W'_l, making it a more robust statistic in the presence of nonuniform background. Note that the mean background intensity $\lambda_{b,l}$ includes stray light, dark counts, and Earth light, and in general is not uniform over the pixels. The mean background intensity for any individual pixel is assumed to be constant over the integration time T_{int}, however. The mean signal beam intensity is modeled as a two-dimensional Gaussian that integrates to λ_s over the entire detector array, with the mean signal intensity over any one pixel, $\lambda_{s,l}$, given by the integral of the two-dimensional Gaussian over the l^{th} pixel boundaries.

Due to bandwidth limitations in designing the readout circuit for the large photon counting detector array, only a limited number of pixel statistics are accessible at any given time. This has led to a design in which the readable pixels are grouped into 4x4 pixel subwindows; 64 of these subwindows are distributed across the 128x128 array, leading to a total of 1024 pixels that may be read out at any given time. The details of how this design choice was made will not be explored here. For each of the k subwindows W_k, $0 \le k \le 63$, we produce two main outputs: a valid flag indicating that the signal is believed to be present in the subwindow, and a centroid estimate of the signal. These subwindow flags and centroids are then processed to give an overall valid flag and centroid estimate over the entire detector array.

2.5.1 Interface With the Simulation Environment

The detector model and processing of the pixel data are split into two distinct modules inside the simulation. This was done to allow for possible portability of the processing algorithms to a hardware target. The processing module outputs centroid estimates for each spot, uplink and downlink, and a detection flag for the uplink beacon. The centroid data is fed back into the control loops and the detection flag is used in the mode commander to tell it when to transition from mode 1 to mode 2.

The simulation provides the beam positions and intensities to the PCD model. The position and intensity of the uplink, downlink and Earth images are provided. The position of the Earth image is tied to the uplink beam position with an offset that can change due to the rotation of the Earth. We have been using a fixed offset with an offset magnitude of one half the Earth diameter. This should represent the most stressing case in terms of accurate uplink beam centroiding. The position and intensity quantities are sampled at 10 times the integration rate of the detector model to provide the model with information on how these quantities are varying during the integration time. This allows modeling of latencies caused by velocity of the spots since the centroid calculation will give the center of mass of the entire spot trajectory not the location at the end of the integration period. The beam positions are given in terms of x and y pixel coordinates with each signal a vector of 11 elements containing the values of the signal from the current time back to end of the previous cycle. The beam intensities are given in units of photons per second. The downlink and Earth intensities are currently constant but they could also be sampled at 10 times the integration rate if they become variable quantities in future versions of the simulation. Also provided as inputs to the PCD model are the diameter of the Earth in pixel units and an Earth crescent parameter designed to tell the PCD model whether the Earth image is full, half or crescent shaped.

The PCD model takes all of the above information and produces 2 up/down counter measureables and 1 up counter measurement for each pixel in the array. These measurements are passed to the PCD processing module. The PCD processing module also requires a mode flag input, generated from the mode commander, that tells the PCD processing module how to configure the subwindows based on what mode the simulation is in. For modes 2 and 3 the subwindows are moving to track the current position of the uplink and downlink beams. The subwindows must be located to fully capture the spot images within the subwindows. To do this the PCD processing module is given the reference position for each control loop, rounded to the nearest integer. This position is taken as the center of the subwindow inside the PCD processing module. As long as the control error is a small portion of the subwindow size the spot will be contained within the subwindow location.

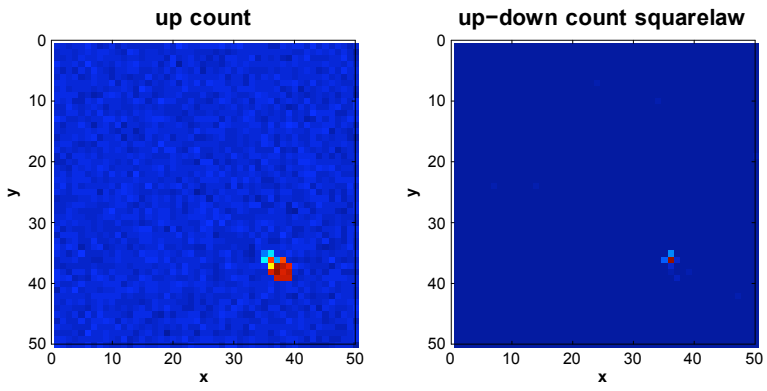

Figure 3. Simulated detector array pixel output levels using two types of detector output statistics, for a case with the uplink signal beacon located along the northwest limb of a uniformly illuminated Earth.

3. ALGORITHMS

3.1 Detection Flag

We denote the outputs of the two up-down counters and one up-counter from the pixel in the i^{th} row and j^{th} column of the k^{th} subwindow by $U_{i,j}(k)$, $V_{i,j}(k)$, and $S_{i,j}(k)$, respectively. The square-law statistic used for subsequent pixel processing is denoted by $W_{i,j}(k) = U^2_{i,j}(k) + V^2_{i,j}(k)$ (or $W_{i,j}(k) = U^2_{i,j}(k) + V^2_{i,j}(k) - 2S_{i,j}(k)$). The k^{th} uplink beacon valid flag $F_R(k)$, indicating that the signal is believed to be present in the k^{th} subwindow, is given by comparing the sum of the square-law statistics, $Z_R(k) = \sum_{i,j \in W_k} W_{i,j}(k)$ to a threshold γ_R, i.e.,

$$F_R(k) = \begin{cases} 1 & Z_R(k) \geq \gamma_R \\ 0 & Z_R(k) < \gamma_R \end{cases} \tag{22}$$

where the detection threshold is given by $\gamma_R = 128NT_s\lambda_b - 32NT_s\lambda_b\Phi^{-1}(PFA_R)$, assuming uniform background and 4x4 pixel subwindows. Here, PFA_R is the probability of false alarm, a quantity that is specified by the user. Note that due to the non-binary nature of the signal detection problem (the beam may be partially in a subwindow), the true probability of false alarm may not match the design parameter PFA_R.

Figure 3 demonstrates the advantage of using the up-down counters to perform signal detection and centroiding rather than simple up-counting only. Here we show the output levels from a 50x50 pixel detector array using the up-counter S, and compare these with the output levels using the up-down counter square-law statistic W. The total signal photon flux intensity is 10^5 photons/sec and is located at the northwest limb of the Earth, which is modeled as a uniform disc four pixels in diameter with flux intensity 5×10^4 photons/sec per Earth pixel. The mean background flux of the non-Earth pixels is set to 10^4 photons/sec per pixel, and all statistics are integrated over 0.01 seconds. We see from this figure that using the pixel up-counts captures the Earth as well as the signal beam, while using the up-down counter square-law statistic results in outputs in which the background level is suppressed, allowing us to isolate the signal beam from the bright Earth light around it. Also note the suppression of noise evident in the background pixels when using the up-down counters.

A further refinement of the detection flag is to pass a number of samples through a logical AND operation to reduce glitches that are possible with the level checking done in Equation (22). Currently 3 samples of the detection flag must be high before the flag is interpreted as high in the mode commander. Another way of doing this consistency check is to pass the square law statistics through a Schmitt trigger element. This will be implemented in updates of the simulation.

3.2 Centroiding

The uplink centroid estimate for subwindow k, $\hat{C}_R(k) = (\hat{x}_R(k), \hat{y}_R(k))$, is calculated as

$$\hat{x}_R(k) = \sum_{j=0}^{N_{columns}-1} (j+0.5) \sum_{i=0}^{N_{rows}-1} W_{i,j}(k) \qquad \hat{y}_R(k) = \sum_{i=0}^{N_{rows}-1} (i+0.5) \sum_{j=0}^{N_{columns}-1} W_{i,j}(k) \tag{23}$$

where $N_{columns}$ and N_{rows} are the number of columns and rows in the subwindow, and $\hat{x}_R$ and $\hat{y}_R$ are given in pixel units.

The up-down counters may not be used to process the downlink beam that is reflected onto the detector array; the average intensity of the downlink signal is not a square wave, but is effectively constant over time scales on the order of the uplink slot time. To calculate the centroid $\hat{C}_T(k) = (\hat{x}_T(k), \hat{y}_T(k))$ of the downlink beam, the up-counters $S_{i,j}(k)$ from the i^{th} row and j^{th} column of the k^{th} subwindow are substituted in place of $W_{i,j}(k)$ in (23).

3.3 Control

A block diagram of all the control loops used in the simulation is shown in Figure 4. Three groupings of control are shown. The inner most loops are the local control loops using the local sensors. These sensor measurements are mapped to joint space using $\mathbf{K}_{pose}$. Three position and three rotational loops are designed with a low bandwidth (30 microhertz). These loops serve only to keep the voice coil actuators centered. Local damping feedback is also added. The damping is implemented on both the translational and rotational degrees of freedom with different gains for each type of motion. The purpose of the damping is to collapse the resonance caused by the lightly damped umbilical stiffness. This is important because the resonant frequency of the platform due to this stiffness is in 0.05 Hz range in the same region where the basebody disturbance has significant power. Without this added electronic damping disturbances could be significantly amplified. The damping transfer function is a simple differentiator with a pole at 10 Hz to make the transfer function causal.

Also shown in Figure 4 are the gimbal loops which can be used for coarse pointing of the transceiver terminal. These loops have a 3 Hz open loop bandwidth. Currently the simulation has no sensor or actuator noise added to these loops so the contribution to the overall pointing jitter from these loop is small. This might actually be more realistic since in practice the gimbals may be locked down during transceiver operations. The third grouping of control are the detector feedback loops. Both the uplink beam and downlink beam loops have a 3 Hz open loop bandwidth. Phase leads are added near the crossover to make these loops stable. Extra gain in the 0.04 Hz range is added to the uplink loops to help reject the basebody disturbance. The uplink loops also have a command path that enables open loop pointing of the platform. Pitch and yaw torques are generated from the mode commander that execute a spiral search of the detector. The spiral filters shown in this signal path attempt to invert the dynamic response of the platform. In pitch and yaw the response of the platform can be approximated by,

$$y_{pcd}(s) = \frac{k_{umbilical_x} * k}{J_{xx}s^2 + cs + k_{umbilical_x}} \tau_{pitch}(s), \tag{24}$$

and,

$$x_{pcd}(s) = -\frac{k_{umbilical_z} * k}{J_{zz}s^2 + cs + k_{umbilical_z}} \tau_{yaw}(s), \tag{25}$$

where $k = 40/1e-7$, $J_{xx} = 0.106$ ($kg-m^2$) and $J_{zz} = 0.083$ ($kg-m^2$) are the inertia of the platform about the pitch and yaw axes, $c = 0.1$ ($Nm/(rad/sec)$) is the electronic damping added to both the pitch and yaw DOF and $k_{umbilical_x} = 0.0003098$ (Nm/rad) and $k_{umbilical_z} = 0.0003117$ (Nm/rad) are the stiffness of the umbilical in the pitch and yaw directions. The outputs of these transfer functions are in units of pixels. The inverse of these transfer functions, with two poles added near 10 Hz, are used in the design of the spiral filters to keep the gain of the open loop command path unity at all frequencies below 10 Hz. These transfer functions are also used to aide in the design of the uplink beam loops.

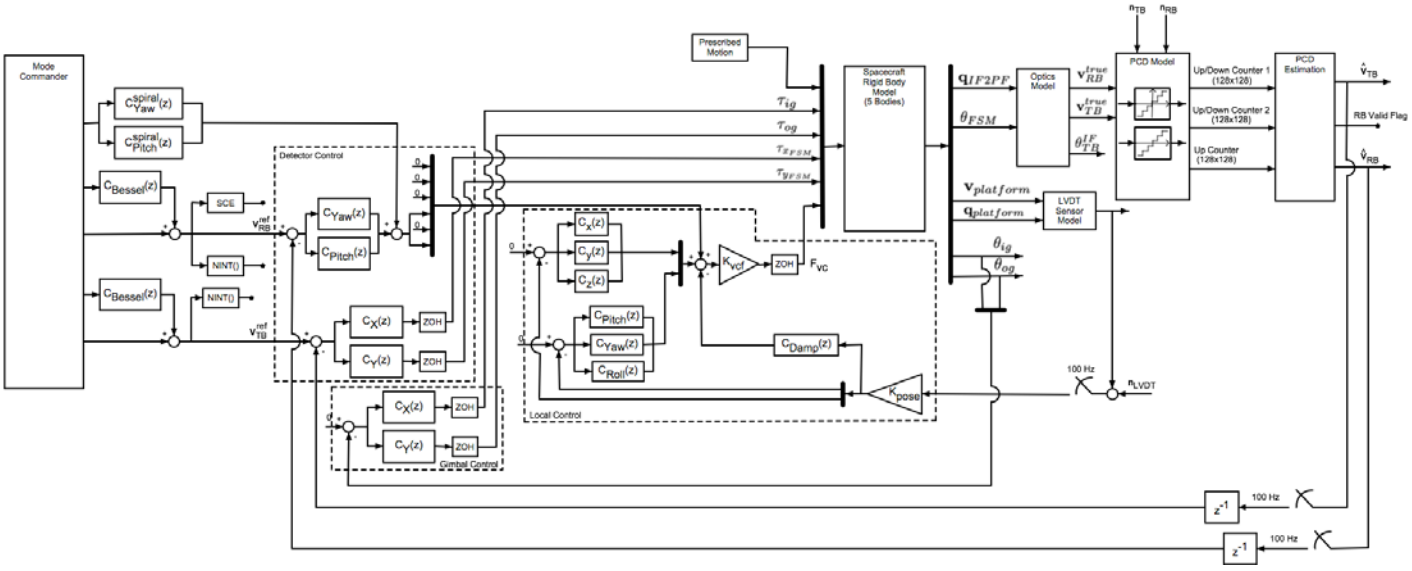

Figure 4. Optical communication control loops. Platform, gimbal and detector feedback are used to control the optical transceiver.

The spiral search trajectory used in mode 1 is designed in the detector space. If we let s_{max} denote the path length velocity of the spiral in pixels per second and g the separation between consecutive loops of the spiral in pixels, the trajectory in pixel coordinates can be obtained from,

$$x_{pcd} = r\cos(\theta) \tag{26}$$

$$y_{pcd} = r\sin(\theta) \tag{27}$$

where,

$$r = \frac{g}{2\pi}\theta \tag{28}$$

and θ is obtained from integrating the following nonlinear differential equation,

$$\dot{\theta} = \frac{2\pi s_{max}}{g}\sqrt{\frac{1}{1+\theta^2}}. \tag{29}$$

We also see a number of Bessel filters in Figure 4 that are used to simply profile in changes in the uplink and downlink focal plane reference positions. This allows smooth transitions during transits of the spot locations. Prior to turning on the downlink beam the basebody disturbance could easily shake the FSM and cause the downlink spot to be in an unpredictable location. This could prevent the downlink loop from being closed without using additional detection procedures. This problem can be avoided by having a passively stiff FSM design. Using the simulation we found that anything with a stiffness above 10 Hz seems to keep the downlink spot with a pixel of its nominal position. This argues for a PZT stage FSM since these mechanisms are normally very stiff. Moreover, the strokes required are compatible with PZT elongations on the order of 7 - 15 microns which is a standard PZT stroke. Voice coil FSMs with soft, low frequency, flexured mounts have excessive stroke capability and are too sensitive to vibrational disturbances.

3.4 Mode Commander

The mode commander is used to switch between operational states of the simulation. In the initial mode, mode 1, the mode commander reads the uplink beacon valid flag provided by the PCD processing module. This uplink valid flag is formed from the subwindow valid flags described in Section 3.1 and is given by

$$F_R = F_R(k^*), \qquad k^* = \arg\max_k \{Z_R(k)\} \tag{30}$$

i.e., the valid flag is equal to the subwindow flag corresponding to the largest subwindow detection statistic $Z_R(k)$. If the valid flag is not asserted a spiral search for the uplink beacon is performed using the platform actuators. As mentioned in Section 1, the simulation assumes there has been some prior placement of the platform using some combination of spacecraft and gimbal pointing. The accuracy of this placement operation is limited by the star tracker. The end of life (EOL) accuracy of a typical star tracker is 120 arc seconds (1-σ) or equivalently 75 pixels which could actually result in the uplink beacon being placed off the 128x128 pixel focal plane array. In either case, the spiral search should result in eventual detection of the uplink beacon by one of the 64 mode 1, 4x4 pixel, subwindows. Once detection is made the spiral is paused, the reference command for the uplink beacon control loop is set the estimated centroid at the time of detection and the uplink beacon loop is closed. The centroid estimate in Mode 1 is given by $\hat{C}_R = (\hat{x}_R, \hat{y}_R)$, where

$$\hat{x}_R = \hat{x}_R(k^*) + \delta_x(k^*), \qquad \hat{y}_R = \hat{y}_R(k^*) + \delta_y(k^*) \tag{31}$$

where $\hat{x}_R(k)$ and $\hat{y}_R(k)$ are the coordinates of the subwindow centroid estimate given in (23) and $k^* = \arg\max_k\{Z_R(k)\}$. The offsets $\delta_x(k^*)$ and $\delta_y(k^*)$ convert the subwindow centroid coordinates to centroid coordinates over the entire detector array.

Once the uplink beacon loop is closed, mode 2 begins, in which the subwindows are coalesced and centered at the nearest integer of the reference command pixel. In this mode only a subset of the 64 available subwindows are required. An odd array of subwindows is used so that the center of the array and hence the uplink spot is in the center of one of the subwindows. The size of the subwindow array must be big enough to capture the initial uncertainty in the centroid estimate. This error can be quite large, several pixels, due to the fact that the uplink spot is nominally detected before it enters a subwindow and the centroid estimate is based only on pixels within the subwindow. Generally a 3x3 array of 4x4 pixel subwindows should be more than big enough to overcome this uncertainty. Once in mode 2, the uplink beacon reference command is adjusted to drag the spot from its detection location to a desired pixel location on the focal plane. During this transit a number of factors influence pointing jitter. The uplink beam control loop must contend with basebody disturbances, centroid noise within the bandwidth of this loop, and granularity of the focal plane which effects centroid measurement accuracy. Since the spot size is small relative to the pixel size the latter issue is important in this application. The centroiding algorithm will lose sensitivity to the true spot location when it is centered within a pixel. At a pixel boundary the sensitivity is recovered. During mode 2, the detector array signal processor continues to calculate subwindow valid flags and centroid estimates, outputting an overall valid flag and centroid estimate. The overall valid flag is given by

$$F_R = \max\{F_R(k)\}, \tag{32}$$

i.e., the overall valid flag is high if any of the subwindow flags are high. The overall centroid estimate is given by

$$\hat{x}_R = \sum_k F_R(k)(\hat{x}_R(k) + \delta_x(k)), \qquad \hat{y}_R = \sum_k F_R(k)(\hat{y}_R(k) + \delta_y(k)), \tag{33}$$

i.e., the overall centroid is the centroid of the valid subwindow centroid estimates.

As the reference command reaches its final destination the mode commander switches to mode 3 where only a single subwindow is used in the uplink beacon control loop. At this time the downlink laser is turned on and its control loop with the FSM is closed. A point ahead angle is calculated and a new reference command for the downlink beacon is profiled in. Once mode 3 has positioned the downlink beam the jitter performance of both the downlink and uplink beams can be assessed. At this point, temporal tracking can commence and uplink command and data channel demodulation can take place.

4. SIMULATION RESULTS

As a means of demonstrating the type of analysis that can be performed with the simulation we show the focal plane trajectories and beam jitter for MRO orbit disturbance with the 8 beam scintillation data. As shown in Figure 5a the simulation starts with the uplink beam (blue data) near the center of the detector. The platform spiral maneuver and disturbance combine to move the the uplink beam until it hits one of the mode 1 subwindow locations. It is detected just outside the subwindow and the estimated centroid location is used to close the uplink

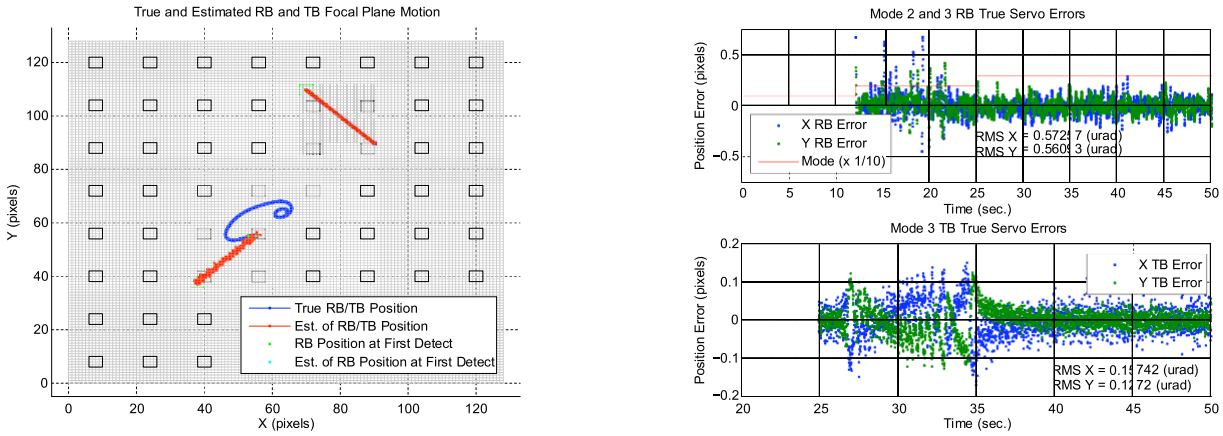

(a) (b)

Figure 5. (a) Uplink and downlink focal plane trajectories for the simulated acquisition sequence. Detector array subwindows are shown in the mode 1 configuration. Final mode 3 subwindow tracking locations are shown as the green subwindows. Mode 2 subwindow configuration is not shown. (b) True RB and TB focal plane jitter after detection of the uplink beam (top subplot) and turning on of the downlink beam (bottom subplot).

loop with a reference command set equal to the first centroid estimate. The reference command is then slowly changed to drag the uplink spot to its final target location on the focal plane. This position is highlighted by the green subwindow on the lower left of the focal plane image. Once the uplink spot reaches this position, the downlink beam is turned on and its control loop is closed with the FSM. To implement the point ahead angle necessary for this beam, a new target location is profiled in. The final target position is again highlighted with the green subwindow in the upper right of the focal plane. In Figure 5b we plot the difference between the reference spot position and the true spot position for both the uplink and downlink beams. This signal is available since the simulation has access to the true beam positions. These signals are plotted for the segment of time after the respective loops are closed. For the uplink beam this is during modes 2 and 3 and for the downlink beam this is during mode 3 only. Note that for both of these data sets the jitter during transit of the beam is greater than during station holding. This is due to the granularity in the focal plane centroid measurement mentioned in Section 3.4. Imagine that the spot size was infinitesimal then the centroid measurement would only change at pixel boundaries and would do so with a quantization of one pixel. On the other hand if the image where several pixels in diameter the centroid measurement would vary smoothly. The jitter after transit for both the uplink and downlink beams is labeled on each subplot. The requirement for the uplink beam is 2.0 microradians per axis (1σ) which is met with an RMS value for each axis of roughly 0.56 microradians. The 2.0 microradian requirement is based on keeping the uplink spot within the linear range of a pixel "quadcell" with each pixel being 8.0 microradians in width. The requirement for the downlink pointing jitter is 0.9 microradians, 1σ, per axis. This requirement is based on maintaining the signal level at the Earth station for a downlink beamwidth of 7.0 microradians. Looking at Figure 6a we see that the inertial downlink beam jitter is 0.55 microradians, 1σ for one axis and 0.51 microradians, 1σ, for the second axis. This again meets the requirement. Note that this inertial beam jitter is comprised of jitter relative to the platform, e.g. Figure 5b (bottom subplot), and a component from the platform jitter, which is much bigger. The jitter relative to the platform is small due to the much larger beam flux used for the downlink beam. It is illustrative to look at the top subplot in Figure 6a. In this figure we can see that during mode 1 the downlink beam direction is following the platform which is moving due to both the spiral search and disturbance. During mode 2, the platform loop is closed and slewed to a target location which is seen as the smooth transition of the downlink direction during this segment of the plot. During mode 3 the downlink beam direction is again smoothly moved but this time with the FSM instead of the platform.

In Figure 6b the PSD of the uplink beam centroid noise is plotted. This data is produced by subtracting the estimated centroid from the true spot position. We see in Figure 6b that the result is white with an amplitude

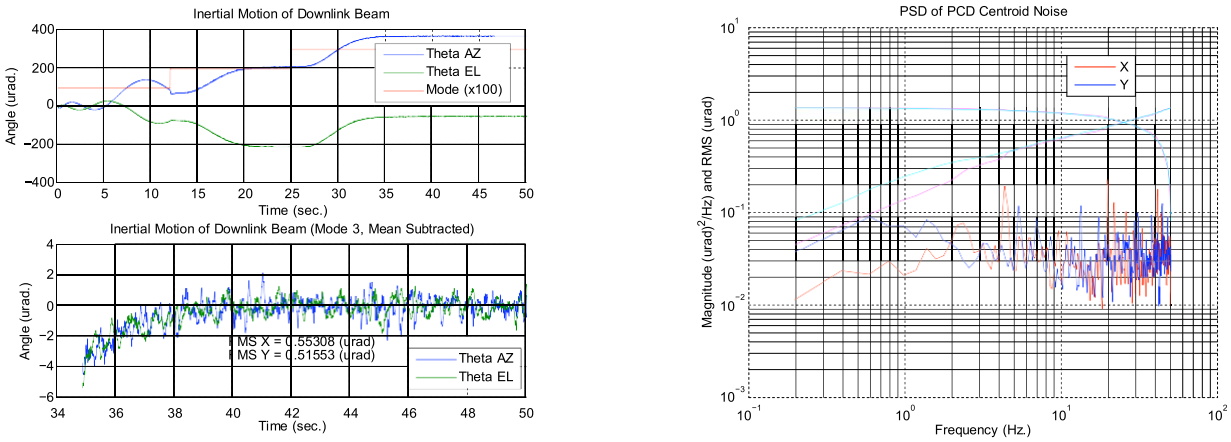

(a) (b)

Figure 6. (a) Inertial motion of the downlink beam during all three modes (top subplot) and after settling in mode 3 (bottom subplot). (b) PSD of the uplink beam centroid noise.

of 0.0382 microradians squared per Hertz, per channel. The amount of centroid noise within the closed loop bandwidth of the uplink loop will cause unwanted jitter of the platform. Since the bandwidth of the uplink loop is 5 Hz we can expect the RMS jitter in this loop due to sensor noise to be $\sqrt{0.0382 * 5} = 0.437$ microradians, or almost 80 percent of the total uplink loop jitter shown in Figure 6b. Thus the primary factor limiting pointing performance is the lack of photons in the uplink spot and poor signal to noise ratio. Note that the poor signal effects both the uplink jitter and downlink jitter since the inertial downlink beam is tied to the platform motion.

5. FUTURE WORK

Several design changes can be made to improve the centroid estimates and pointing performance. In the area of signal processing if the phase of the modulated beacon signal could be determined the signal level at each pixel could be calculated without the square law statistic described in Section 3.1. This would avoid squaring of the noise and reduce the amplitude of the PSD in Figure 6b. Determining this phase is something that could be achieved with a simple phase lock loop circuit. Using a smaller tracking subwindow is also likely to pay big dividends in terms of better centroid estimates. Moving from a 4x4 subwindow to a 2x2 subwindow is possible since the simulation shows that the jitter is well contained within a 2x2 region. Using 4 pixels instead of 16 to calculate centroids will reduce the centroid noise since the spot image is small.

In the area of estimation, the uplink centroid measurement could be smoothed substantially by using models of the platform actuator and basebody disturbance. The estimator would take in measurements of the pitch and yaw control inputs and uplink beam centroids and produce a cleaned up centroid estimate. Using this estimate in the uplink beam control loop would reduce both uplink jitter and downlink jitter since reducing platform jitter effects both beams. The response of the centroid position to pitch and yaw torque commands is well described by simple second order transfer functions. These transfer functions depend on the inertia of the platform in these two directions as well as the local damping feedback and umbilical stiffness. The estimation problem is complicated, however, by the relatively poor knowledge of the basebody disturbance and in how much of this disturbance get through the isolator. This problem can be addressed, however, with multiple model adaptive estimation.[14] By using a family of disturbance models the estimator can use the prediction error of each model to choose the best model within the family. This approach can also address time variation in the disturbance since the estimator will continuously hunt for the best disturbance model. Thus, during orbital events that cause big basebody motions, the bandwidth of the estimator will be extended, and less smoothing will result, to better track these events. An estimator of this sort could also be used to replace a platform mounted IMU in applications that demand tracking of dim targets.

The simulation currently assumes some calculation has been done for the point ahead for the downlink beam. This calculation is somewhat complex due to the amount of information needed. It would require the ephemeris velocities of both the spacecraft and Earth station. One would also have to have knowledge of the focal plane to sky coordinates calibration so that the correct pixel location can be determined from a desired inertial downlink direction. In addition the inertial roll about the direction of the uplink beam is required since this will effect the clock angle of the downlink beam due to it being offset by the point ahead angle. Some sort of estimation scheme is needed for the roll which conceivably could be reconstructed from spacecraft attitude measurements and platform local sensor measurements. Including a virtual solar system in the DOT simulation would enable the development of point ahead algorithms and performance assessment of these algorithms against requirements.

ACKNOWLEDGMENTS

The work described in this paper was carried out at the Jet Propulsion Laboratory, California Institute of Technology, under contract with the National Aeronautics and Space Administration.

REFERENCES

[1] Jeganathan, M., Portillo, A., Racho, C. S., Lee, S., Erickson, D. M., DePew, J., Monacos, S., and Biswas, A., "Lessons Learned from the Optical Communications Demonstrator (OCD)," *Proc. of SPIE* **3615** (1999).

[2] Regehr, M. W., Biswas, A., Kovalik, J. M., and Wright, M. W., "Pointing Performance of an Aircraft-to-Ground Optical Communications Link," *Proc. of SPIE* **7814** (2010).

[3] Roberts, W. T. and Wright, M. W., "Deep-space Optical Terminals (DOT) Ground Laser Transmitter (GLT) Trades and Conceptual Point Design," *The Interplanetary Network Progress Report* **42-183**, 1–13 (November 15 2010).

[4] Fujiwara, Y., Mokuno, M., Jono, T., Yamawaki, T., Arai, K., Toyoshima, M., Kunimori, H., Sodnik, Z., Bird, A., and Demelenne, D., "Optical Inter-orbit Communications Engineering Test Satellite (OICETS)," *Acta Astronautica* **61**, 163–175 (March 2007).

[5] Farr, W., Regehr, M., Wright, M., Sheldon, D., Sahasrabudhe, A., Gin, J., and Nguyen, D., "Overview and Design of the DOT Flight Laser Transceiver," *The Interplanetary Network Progress Report* **42-185**, 1–31 (May 15 2011).

[6] Burnside, J. W., Murphy, D. V., Knight, F. K., and Khatri, F. I., "A Hybrid Stabilization Approach for Deep-Space Optical Communications Terminals," *Proceedings of the IEEE* **95-10**, 2070–2081 (October 2007).

[7] Biswas, A., Hemmati, H., Piazzolla, S., Moision, B., Birnbaum, K., and Quirk, K., "Deep-space Optical Terminals (DOT) Systems Engineering," *The Interplanetary Network Progress Report* **42-183**, 1–38 (November 15 2010).

[8] Sannibale, V., Ortiz, G., and Farr, W., "A Sub-hertz Vibration Isolation Platform for a Deep Space Optical Communication Transceiver," in [*Free-Space Laser Communication Technologies XXI*], Hemmati, H., ed., *Proc. of SPIE* **7199** (2009).

[9] Farr, W., Regehr, M., Wright, M., Sheldon, D., Sahasrabudhe, A., Gin, J., and Nguyen, D., "Overview and Design of the DOT Flight Laser Transceiver," *The Interplanetary Network Progress Report* **42-185**, 1–31 (May 15 2011). http://ipnpr.jpl.nasa.gov/progress_report/42-185/185D.pdf.

[10] Regehr, M., "Status and Plans: LPV Analysis, Flywheel Mode, and RFI," Tech. Rep. (Powerpoint Presentation), Jet Propulsion Laboratory (2011).

[11] Regehr, M., Ortiz, G., and Sannibale, V., "DOT Concept Review: FLT Pointing, Acquisition and Tracking," Tech. Rep. (Powerpoint Presentation), Jet Propulsion Laboratory (2010).

[12] Shields, J. F., "Analysis of MRO Orbit and Cruise Pointing Data," Tech. Rep. EM-3411-11-001, Jet Propulsion Laboratory (2011).

[13] Piazzolla, S. (2011). Private communication.

[14] Maybeck, P. S., [*Stochastic Models, Estimation, and Control, Volume 1, 2 and 3*], Mathematics in Science and Engineering, Academic Press, New York (1979).